

Phase-dependent electronic structure of two-dimensional Ag layers at the graphene/SiC interface

Sawani Datta,^{1,*} Boyang Zheng,^{2,3} Arpit Jain,⁴ Kathrin Küster,¹
Joshua A. Robinson,^{3,4,5} Vincent H. Crespi,^{2,3,4} and Ulrich Starke¹

¹*Max-Planck-Institut für Festkörperforschung, Heisenbergstraße 1, 70569 Stuttgart, Germany*

²*Department of Physics, The Pennsylvania State University, University Park, PA 16802, USA*

³*2-Dimensional Crystal Consortium, The Pennsylvania State University, University Park, PA 16802, USA*

⁴*Department of Materials Science and Engineering,*

The Pennsylvania State University, University Park, PA 16802, USA

⁵*Center for Atomically Thin Multifunctional Coatings,*

The Pennsylvania State University, University Park, PA 16802, USA

Intercalation at the graphene/SiC interface provides a controlled route to stabilize atomically thin layers with properties distinct from their bulk counterparts. In this platform, the structure and stability of the intercalated phase depend sensitively on the defect landscape of the starting substrate. For intercalated two-dimensional silver at the graphene/SiC interface, two phases have been observed: a phase epitaxial to the SiC lattice, called $\text{Ag}_{(1)}$, readily obtained following the conventional intercalation method under ultra-high-vacuum conditions and extensively characterized, and a more densely packed phase, called $\text{Ag}_{(2)}$, which has remained largely unexplored. Here we report an *in situ* ultra-high-vacuum preparation method of the second phase intercalated at the graphene/SiC interface; this phase previously was prepared via high-pressure confinement heteroepitaxy. Low-energy electron diffraction shows that $\text{Ag}_{(2)}$ is rotated by 30° relative to the SiC lattice and forms supercells, in contrast to the (1×1) epitaxial relation of $\text{Ag}_{(1)}$ with SiC. High-resolution angle-resolved photoemission spectroscopy reveals a more complex $\text{Ag}_{(2)}$ band dispersion compared to the $\text{Ag}_{(1)}$, as a consequence of the modified Ag-Si interaction in the denser phase. In density functional theory calculations, by defining the unfolding entropy which, in a quantified way, finds that the band structure of $\text{Ag}_{(2)}$ is more suitable to be unfolded to the SiC primitive cell, and the resulting unfolded band dispersion is in great agreement with the experimental data. We further show that the different intercalated Ag phases tune the electronic properties of the overlying quasi-free-standing graphene layer differently: compared with $\text{Ag}_{(1)}$, $\text{Ag}_{(2)}$ yields an ~ 1.75 times higher charge carrier density and modifies the charge-plasmon interaction of the graphene layer, indicating a change in effective screening at the interface.

I. INTRODUCTION

Quantum confinement in reduced-dimensional systems is a central topic in materials science, driven by both fundamental questions [1–5] and technological prospects [6–9]. In particular, reducing the film thickness to the atomic limit constrains electron motion and reshapes the electronic density of states, which can markedly modify chemical reactivity, mechanical response, and optical properties relative to the bulk [10–12]. From a fundamental perspective, atomically thin layers can host emergent phenomena absent in their three-dimensional counterparts, including altered screening, enhanced many-body interactions, and symmetry-driven electronic instabilities [13–16]. A key challenge, however, is achieving and maintaining the structural and chemical stability of such two-dimensional (2D) phases, which are often metastable [17–19] and strongly influenced by the choice of substrate, interface bonding, and environmental exposure [20, 21]. In this context, intercalating a two-dimensional material at the graphene/SiC interface offers a practical way to improve stability. The SiC substrate can help stabilize an

intercalated layer by providing interfacial bonding and an ordered template for growth, while the graphene overlayer acts as a largely inert, atomically thin cap that shields the intercalated film from the environment and lowers its chemical reactivity [21–31].

As noted above, substrate templating—and thus the quality and defect landscape of the starting substrate—plays a central role in stabilizing intercalated interfacial layers. In this context, early studies showed that 2D-Ag and 2D-Ga intercalated at the graphene/SiC interface using the confinement heteroepitaxy (CHet) approach (performed under elevated pressure) [32] can form two distinct monolayer (ML) phases [33, 34]. Subsequent systematic work on CHet-grown Ag-MLs demonstrated that the occurrence of these phases depends extensively on the type and density of defects in the initial substrate [35]. In particular, substrates dominated by line and boundary defects tend to yield an Ag-ML, with a (1×1) epitaxial relationship to the SiC lattice, which we refer to as the $\text{Ag}_{(1)}$ phase. In contrast, increasing the density of sp^3 -type defects favors formation of a denser Ag-ML [35]. In this $\text{Ag}_{(2)}$ phase, Ag adopts a more complex relationship with the SiC unit cell and is rotated by 30° with respect to SiC [35]. These two phases of Ag also exhibit significant differences in the optical responses, visi-

* s.datta@fkf.mpg.de

ble electronic absorption and sensing applications [34–36]. Combined experimental and theoretical studies further indicate that $\text{Ag}_{(2)}$ is thermodynamically more stable, and a time-dependent transformation from $\text{Ag}_{(1)}$ to $\text{Ag}_{(2)}$ has been reported [35].

While the CHet method enables the formation of intercalated layers over large areas at the graphene/SiC interface [32, 37], the present work focuses on an *in situ* ultra-high vacuum (UHV) route that is directly compatible with stepwise preparation and immediate surface-sensitive characterization by LEED, ARPES, and XPS without breaking vacuum. In this sense, CHet and UHV intercalation provide complementary routes: CHet is well suited for scalable synthesis, whereas UHV enables the *in situ* structural and electronic property measurements to avoid any undesired phase transitions in the ambient condition [35]. Using standard UHV intercalation (Ag deposition on zero-layer graphene followed by annealing), the $\text{Ag}_{(1)}$ phase is typically obtained [14, 24]. To our knowledge, however, preparation of $\text{Ag}_{(2)}$ entirely under UHV conditions has not been demonstrated so far. Here we present the first UHV preparation route that yields $\text{Ag}_{(2)}$ intercalation at the graphene/SiC interface, enabled by deliberately increasing vacancy-type defects through an additional intercalation step as described in the main text. We then provide a detailed experimental and theoretical investigation of the structural and electronic properties of atomically thin 2D- $\text{Ag}_{(2)}$. The structural characteristics are determined by low-energy electron diffraction (LEED) and supported by density functional theory (DFT) calculations. The electronic properties are investigated using high-resolution angle-resolved photoemission spectroscopy (ARPES) in combination with DFT band-structure calculations. The calculated band structure based on the proposed structural model for $\text{Ag}_{(2)}$ [35] reproduces the key features of the ARPES spectra. As expected, $\text{Ag}_{(2)}$ exhibits a more complex electronic structure than $\text{Ag}_{(1)}$, accompanied by a clear shift in the Ag core-level spectrum. We further show that the phase-selective intercalation of Ag at the graphene/SiC interface provides a route to tune the *n*-type doping of quasi-free-standing monolayer graphene (QFMLG) and modifies the electron-plasmon coupling in graphene via proximity effects. Finally, we demonstrate that supercell formation between $\text{Ag}_{(2)}$ and graphene, produces replica features in ARPES, consistent with superstructure signatures observed in the LEED.

II. METHODS

A. Sample preparation

For the preparation of graphene, we start with a mechanically polished and *n*-doped 6H-SiC (0001) substrate (from SiCrystal GmbH) with a miscut of $< 0.1^\circ$ with respect to the $\{0001\}$ plane. Following a chemical HF cleaning, to achieve an atomically flat surface for homogeneous graphene growth, the polishing scratches were

removed by annealing the sample in an 800 mbar hydrogen atmosphere at about 1405°C for 20 minutes [38, 39]. The graphitisation of the SiC sample was performed in the same reactor under an Ar atmosphere (800 mbar pressure) by sublimating the Si atoms [40] through heating the sample to $\sim 1445^\circ\text{C}$ for 4.5 minutes. This technique results in the formation of a graphene buffer layer (zero layer graphene or ZLG) with terraces a few microns wide [41, 42]. The ZLG exhibits the $(6\sqrt{3} \times 6\sqrt{3})R30^\circ$ reconstruction relative to the underlying SiC substrate originating from the lattice mismatch [41, 43]. Due to the presence of the partial sp^3 bonding at the ZLG/SiC interface, ZLG would not show any Dirac cone dispersion in the ARPES data [41, 43].

For $\text{Ag}_{(1)}$ intercalation, Ag was deposited for 30 min (nominal rate $1 \text{ \AA}/\text{min}$) onto a ZLG sample held at 400°C , followed by post-annealing at 600°C and 650°C for 30 min at each temperature. A second deposition step with the same Ag dose was then carried out at 400°C , followed by annealing from 600°C to 700°C in 50°C steps, holding for 30 min at each temperature. This two-step preparation protocol follows the previously reported refined procedure [14] for getting sharper Ag and graphene bands. Although the annealing temperatures and times were kept essentially the same, the present samples were prepared in a different preparation chamber with a modified experimental setup. In particular, we used electron-beam heating instead of direct plate heating as the reported one, and the evaporator-to-sample distance also differed. Nevertheless, the characteristic LEED signatures and the electronic band structures of both the Ag-ML and the resulting QFMLG are well reproduced. We observe a slight shift of the Ag-derived bands to higher BE compared to ref.[14].

For $\text{Ag}_{(2)}$, Ag was first evaporated for 20 min (nominal rate $1 \text{ \AA}/\text{min}$) onto the ZLG sample held at 450°C , followed by sequential annealing at 600°C , 630°C , and 650°C for 20 min at each temperature. Up to this point, the procedure is essentially identical to the one-step procedure used in ref.[24] for $\text{Ag}_{(1)}$ intercalation, and the LEED pattern likewise shows the characteristic $\text{Ag}_{(1)}$ -QFMLG signature: enhanced graphene (1×1) spots and suppressed $(6\sqrt{3} \times 6\sqrt{3})R30^\circ$ features (see Supplementary Information (SI), section A, Fig. S1 (a) and (b)). As mentioned above, to obtain the $\text{Ag}_{(2)}$ phase in UHV, the defect landscape of the initial substrate is modified, in particular by promoting additional vacancy-type defects [32, 44]. To achieve this, we introduced one cycle of Ag deintercalation followed by re-intercalation. Deintercalation was carried out using Pb, taking advantage of the fact that the heavier Pb atoms can replace intercalated Ag at the interface. Specifically, Pb was deposited onto the $\text{Ag}_{(1)}$ -QFMLG sample at room temperature for 5 min (nominal rate $4 \text{ \AA}/\text{min}$), followed by annealing at 400°C and 500°C for 30 min at each temperature [25]. These steps result in complete substitution of Ag by Pb, yielding Pb-QFMLG (cf. SI, section A, Fig. S1 (c)), in agreement with the established LEED and ARPES signatures

reported previously [25, 45]. In the subsequent Ag intercalation step, Ag was deposited onto the Pb-QFMLG sample at 450 °C for 30 min (nominal rate 1 Å/min), followed by annealing at 600 °C, 650 °C, and 700 °C for 30 min at each temperature. Notably, in separate preparations we found that omitting the initial Ag-intercalation step (i.e., starting directly from Pb-QFMLG) still yields the same final Ag₍₂₎ phase; the first Ag-intercalation cycle therefore appears to mainly create additional defect/entry channels that facilitate the subsequent Pb intercalation.

Thus, the key practical difference between Ag₍₁₎ and Ag₍₂₎ in UHV is the starting substrate: Ag₍₁₎ is obtained by intercalating Ag into ZLG, whereas Ag₍₂₎ is obtained by intercalating Ag into Pb-QFMLG. Qualitatively, this can be understood by noting that a higher density of vacancy-type defects in Pb-QFMLG, from the process of Pb intercalation, likely provides favorable entry channels and nucleation sites for stabilizing Ag₍₂₎ intercalation [45, 46]. In addition, because Pb forms a supercell with graphene [25, 28, 45, 47], associated boundary defects could further promote [48] the formation of the Ag₍₂₎ phase. A quantitative characterization of the defect density in Pb-QFMLG is beyond the scope of the present work. Future studies could address this point and explore whether other intercalated QFMLG systems can serve as alternative starting substrates for stabilizing the Ag₍₂₎ phase.

B. Characterization

We investigated the initial sample quality and analyzed the structural information *in situ* by LEED using an Er-LEED system (SPECS GmbH). The experimental photoemission spectroscopy (PES) data of the Ag₍₂₎ intercalated sample presented in this work were acquired at the Bloch beamline of the MAX IV synchrotron facility (Lund, Sweden) [49]. On the Ag₍₁₎ intercalated sample, PES was measured at the 1² end-station of UE112 PGM-2a-1² beamline at BESSY II, Helmholtz-Zentrum Berlin, Germany [50]. To prevent air exposure during transport, the samples were transferred in a Ferrovac UHV suitcase with a base pressure below 1×10^{-9} mbar. All PES measurements were carried out at a sample temperature ≈ 20 K. At the Bloch beamline, PES measurements were performed using a DA30-L hemispherical analyzer (Scienta Omicron GmbH). Synchrotron radiation with photon energies in the range 40–180 eV was used for ARPES, while photon energies of 180–650 eV were employed for core-level x-ray photoemission spectroscopy (XPS). The best overall energy resolution achieved in ARPES was approximately 18 meV. At the 1² end-station, ARPES measurements were done using an R8000 hemispherical analyzer (Scienta Omicron GmbH). Measurements were performed with photon energies of 110 eV and 40 eV, and the best overall energy resolution achieved was 20 meV.

C. DFT calculation

The calculations are done by the Vienna *ab initio* simulation package (VASP) [51–54], using the projector augmented wave (PAW) method [55] and the Perdew-Burke-Ernzerhof (PBE) exchange-correlation functional [56]. The computational unit cells have 3 layers of SiC stacked in the ABC-form (consistent with the 6H-SiC) whose lattice constant in the *ab*-plane is 3.096 Å, and the *z*-dimension of the cell is 20 Å to include enough vacuum preventing interactions between the periodic images. The bottom layer is passivated by H atoms and no graphene cap is included. For Ag₍₁₎, we used the ideal (1 × 1) registry of Ag on top of the hollow-site of the topmost SiC layer. For Ag₍₂₎, we have (3√3 × 3√3) (in total 27) Ag atoms on top of a (5 × 5) SiC supercell. The cutoff energy is 450 eV, the self-consistent field (SCF) convergence criterion is 1.4×10^{-8} eV/atom, and the force convergence criterion is 0.01 eV/Å with D3 van der Waals correction [57, 58]. The k-point samplings are Γ -centered $13 \times 13 \times 1$ ($51 \times 51 \times 1$) for the self-consistent (non-self-consistent) calculations for Ag₍₁₎, and Γ -centered $3 \times 3 \times 1$ ($10 \times 10 \times 1$) for Ag₍₂₎. The band unfolding [59] is done with the `VaspBandUnfolding` code [60]. Since we don't have the graphene cap, or take into account of any charge transfer effect, the extra electrons from Ag in Ag₍₂₎ will be in the conduction band, while experimentally the Fermi level is in the gap. In addition, our calculations do not include any correction for the underestimated band gap problem in DFT [61]. Therefore, we ignore the conduction bands when comparing with ARPES.

III. RESULTS AND DISCUSSION

A. Structural and chemical characterization of Ag₍₂₎ intercalated QFMLG

We begin with a structural comparison of the two intercalated 2D-Ag phases using LEED. Figures 1(a) and 1(b) show LEED patterns of the Ag₍₁₎- and Ag₍₂₎-intercalated samples, respectively, recorded at the surface-sensitive electron energy of 70 eV [62]. For Ag₍₁₎ (Fig. 1(a)), the pattern is dominated by graphene (1 × 1) reflections (grey circle), while the SiC (1 × 1) spots (green circle) are comparatively weak. The $6\sqrt{3}$ spots characteristic of the ZLG buffer-layer reconstruction are strongly suppressed after intercalation, consistent with decoupling of graphene from the SiC surface and the removal of the interfacial reconstruction [21, 24, 41].

For the Ag₍₂₎ sample (Fig. 1(b)), it exhibits, in addition to the primary diffraction spots (graphene (1 × 1) and SiC (1 × 1) spots indicated by the grey and green circles respectively), two distinct sets of replica spots (highlighted by pink and blue dashed box in Fig. 1(b)) arising from supercells formation. These supercells can be clearly seen in the top-view schematics of the SiC/Ag₍₂₎/graphene stacking shown in Fig. 1(c), based on the structural model

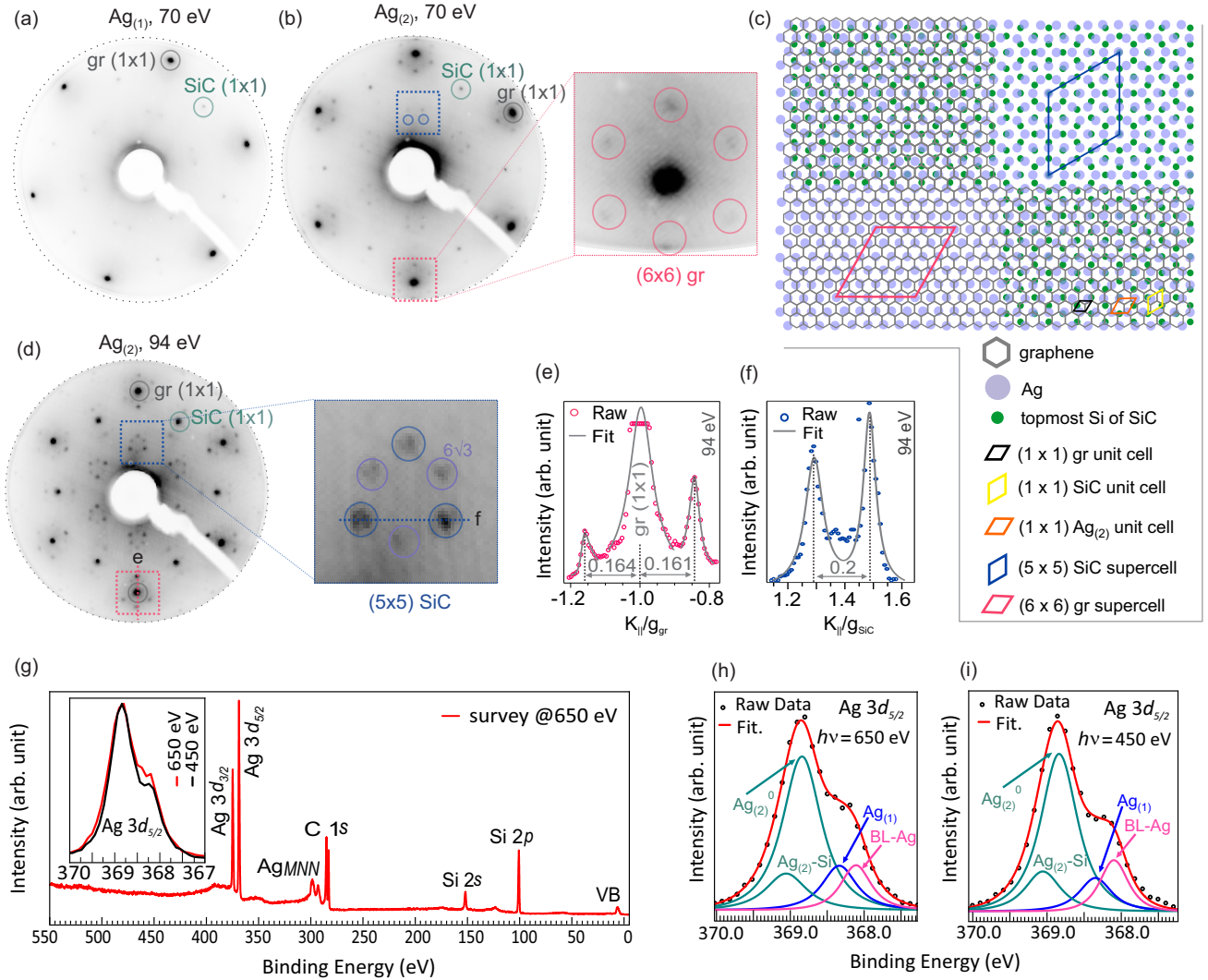


FIG. 1. LEED patterns of (a) $\text{Ag}_{(1)}$ -QFMLG and (b) $\text{Ag}_{(2)}$ -QFMLG at 70 eV. The graphene (1×1) and SiC (1×1) spots are indicated by gray and green circles, respectively, in (a), (b), and (d). The (6×6) graphene replica spots are highlighted with pink circles in the enlarged view associated with (b), while the (5×5) SiC replica spots are marked by blue circles. (c) Top-view schematic of the SiC/ $\text{Ag}_{(2)}$ /graphene stacking sequence. Upper left: complete stack, showing the Si atoms (green spheres) of the topmost SiC, $\text{Ag}_{(2)}$ atoms (violet spheres), and the graphene lattice (gray hexagon). Upper right: $\text{Ag}_{(2)}$ on top of Si(C), including the (5×5) SiC supercell (blue rhombus). Lower left: graphene on $\text{Ag}_{(2)}$ with the (6×6) graphene supercell (pink rhombus). Lower right: combined view including all unit cells; the legend is shown at the bottom. (d) LEED pattern of $\text{Ag}_{(2)}$ at 94 eV; the (5×5) SiC replica spots are marked in the corresponding enlarged view. (e, f) Line profiles (raw data: pink/blue open circles; fit: gray solid lines) taken through the (e) (6×6) graphene replicas and (f) (5×5) SiC replicas, along the directions indicated in (d). (g) XPS survey spectrum of $\text{Ag}_{(2)}$ acquired at 650 eV; inset: $\text{Ag } 3d_{5/2}$ region measured at 650 eV (red) and 450 eV (black). (h, i) Fits to the $\text{Ag}_{(2)}$ $3d_{5/2}$ spectra at (h) 650 eV and (i) 450 eV, with the corresponding fit components shown.

of Ref. [35]. The sixfold group of satellites surrounding the graphene (1×1) spot (in the pink box in panel (b) and the associated enlarged view) is from a $\sim (6 \times 6)$ graphene supercell commensurate with a $\sim (5 \times 5)$ $\text{Ag}_{(2)}$ supercell (guided by the pink rhombus in the lower-left quadrant of Fig. 1(c)). The second set, highlighted by the blue circles (in the blue box), is more clearly resolved in a LEED pattern (Fig. 1(d)) with higher energy (94 eV), which is more sensitive to the SiC. These spots correspond to a $\sim (5 \times 5)$ supercell of the SiC substrate, which is commensurate with the $(3\sqrt{3} \times 3\sqrt{3})$ supercell of $\text{Ag}_{(2)}$, as

outlined by the blue rhombus in the upper-right quadrant of Fig. 1(c).

To quantify the supercell periodicities, we performed Lorentzian fits to line profiles passing through the replica spots. Fig. 1(e) shows a fit to a profile through the graphene (1×1) spot and a diagonally opposite pair of the sixfold satellites (profile direction indicated by the pink line in Fig. 1(d)). The average separation of the left and right replica spots from the graphene (1×1) reflection corresponds to 0.163 of the graphene reciprocal-lattice vector (\mathbf{G}_{gr}), indicating an approximately ($6 \times$

6) periodicity (more precisely, (6.1×6.1)) relative to graphene. A corresponding line profile analysis of the second set of replicas (Fig. 1(f), profile direction indicated by the blue line in the enlarged view in panel(d)) yields a separation of 0.2 of the SiC reciprocal surface lattice vector (\mathbf{G}_{SiC}), identifying these spots as the (5×5) SiC grid spots [63]. Overall, the LEED signatures agree well with those reported previously for $\text{Ag}_{(2)}$ prepared using the CHet method [35]. The corresponding replica features observed in ARPES are discussed later in Sec. III F.

From this LEED analysis we conclude that $\text{Ag}_{(2)}$ is rotated by 30° with respect to the underlying SiC lattice and does not form a simple (1×1) epitaxial relation as in $\text{Ag}_{(1)}$, but instead adopts the commensurate relation as described above. Maintaining the (1×1) epitaxy in $\text{Ag}_{(1)}$ implies tensile strain, with an Ag-Ag distance (3.10 \AA) larger than that in bulk Ag (2.88 \AA) [64]. In contrast, the rotated lattice of $\text{Ag}_{(2)}$ has a higher areal Ag density and a shorter Ag-Ag bond of length $\sim 2.98 \text{ \AA}$ [35] to help relieve the strain [35, 64].

To examine the chemical purity of the prepared sample, an XPS survey spectrum acquired with 650 eV photon energy is shown in Fig. 1(g). The survey is dominated by the Ag $3d_{5/2}$ and Ag $3d_{3/2}$ spin-orbit split peak [24, 65], together with the expected C $1s$, Si $2p$, and Si $2s$ emissions [65]. In addition, the Ag MNN Auger features [66] and the valence band signal are clearly observed. Importantly, the O $1s$ [65] signal is not detectable, indicating the absence of measurable air contamination. Furthermore, no Pb $4f$ emission is observed in the binding energy (BE) window of $\sim 135\text{--}143 \text{ eV}$ [25]. Given that the photoionization cross-sections of Ag $3d$ and Pb $4f$ are of comparable magnitude at 650 eV [67], the absence of Pb $4f$ provides strong evidence that Pb has been effectively removed during the preparation. We therefore conclude the above-mentioned preparation method, starting from Pb-QFMLG, yields a chemically clean $\text{Ag}_{(2)}$ -ML at the graphene/SiC interface.

A pronounced photon-energy dependence is observed in the Ag $3d$ core-level line shape when the excitation energy is reduced from 650 eV to 450 eV, while keeping the sample position and all other experimental parameters unchanged. As shown in the inset of Fig. 1(g) for the Ag $3d_{5/2}$ region, the main peak maximum remains essentially unchanged, whereas the low-BE shoulder is strongly suppressed at 450 eV. To quantify this effect, the Ag $3d_{5/2}$ spectra acquired at 650 eV and 450 eV were fitted using Voigt functions [68] as shown in Fig. 1(h) and 1(i), respectively; for the wide-range fit of the Ag $3d$ spectra, see SI, section B, Fig. S2. By comparing with the literature, we assign the component at $\sim 368.4 \text{ eV}$ to an $\text{Ag}_{(1)}$ -like contribution previously reported for the $\text{Ag}_{(1)}$ phase [35]. The dominant spectral weight is attributed to $\text{Ag}_{(2)}$ ⁰, i.e., the in-plane Ag–Ag bonding within the $\text{Ag}_{(2)}$ intercalation layer, while the highest-BE component is assigned to the Ag–Si bonding at the interface with the SiC substrate [35]. The presence of two distinct $\text{Ag}_{(2)}$ bonding components indicates a nonuniform local electronic

environment within the $\text{Ag}_{(2)}$ layer, in contrast to the more homogeneous $\text{Ag}_{(1)}$ phase, which is characterized by a single Ag $3d$ component [24]. We note a systematic BE offset of the $\text{Ag}_{(2)}$ peaks of approximately $\sim 0.3 \text{ eV}$ relative to Ref. [35], which may arise due to slight variations in the local chemical environment and screening. Notably, in the more surface-sensitive 450 eV data, the relative intensity of the peak associated with the $\text{Ag}_{(1)}$ layer as compared to the $\text{Ag}_{(2)}$ components is lower than for 650 eV. This trend is consistent with the simplified model of the exponential attenuation of photoemission intensity with larger depth [62]. Since transmission electron microscopy [35] data indicates that $\text{Ag}_{(1)}$ resides deeper below the graphene overlayer than $\text{Ag}_{(2)}$, the $\text{Ag}_{(1)}$ contribution is more strongly suppressed under surface-sensitive conditions, leading to a lower relative $\text{Ag}_{(1)}$ intensity. As a result, the $\text{Ag}_{(1)}$ contribution is more strongly suppressed in the surface-sensitive measurement, leading to a reduced $\text{Ag}_{(1)}/\text{Ag}_{(2)}$ intensity ratio. The lowest-BE component (BL-Ag) lies close to the reported value for metallic Ag [24]. One possible origin would be non-intercalated Ag residing on top of the graphene; however, such a surface contribution would be expected to increase markedly in the more surface-sensitive 450 eV measurement, which is not observed. We therefore ascribe this low-BE component to a minor phase (or domains) of intercalated Ag with a more metallic local environment. This assignment is discussed further in connection with the last section (Sec. III G).

B. ARPES of $\text{Ag}_{(1)}$ and $\text{Ag}_{(2)}$

Fig. 2(a) presents the electronic band structure of the $\text{Ag}_{(1)}$ phase measured along the $\overline{\Gamma\text{M}_{\text{SiC}}\overline{\text{K}}_{\text{SiC}}\overline{\Gamma}}$ direction. The data were acquired with a photon energy of 110 eV. The corresponding surface Brillouin zones (BZs) of SiC and graphene are superimposed in the constant-energy contour (CEC) data in Fig. 2(b). Consistent with earlier reports (Ref. [24]), the $\text{Ag}_{(1)}$ phase exhibits semiconducting behavior [69] as the valence band maximum (VBM) is at a BE of $0.59 \pm 0.05 \text{ eV}$ below the Fermi level (E_F) at the $\overline{\text{K}}_{\text{SiC}}$ point. That exact value of the VBM is confirmed by the fitting of the energy-distribution curve (EDC) superimposed at $\overline{\text{K}}_{\text{SiC}}$. The dispersion also displays a saddle point feature at the $\overline{\text{M}}_{\text{SiC}}$ point at a BE of approximately 1.60 eV. Along $\overline{\Gamma\text{M}}_{\text{SiC}}$, Ag-derived states show clear hybridization with SiC bulk bands, which become visible near $\sim 2.5 \text{ eV}$ BE. The CEC at 1.60 eV BE in Fig. 2(b) highlights the band topology at the saddle point $\overline{\text{M}}_{\text{SiC}}$, where the contour shows a pronounced hexagonal shape.

Fig. 2(c) shows the electronic band structure of the $\text{Ag}_{(2)}$ phase measured with 110 eV light. Similar to the $\text{Ag}_{(1)}$ phase, $\text{Ag}_{(2)}$ exhibits semiconducting character, with the VBM located well below E_F at the $\overline{\text{K}}_{\text{SiC}}$ point. In contrast to $\text{Ag}_{(1)}$, however, the $\text{Ag}_{(2)}$ -derived band near $\overline{\text{K}}_{\text{SiC}}$ splits into three components, as demonstrated by the EDC extracted at $\overline{\text{K}}_{\text{SiC}}$ and overlaid at the corresponding

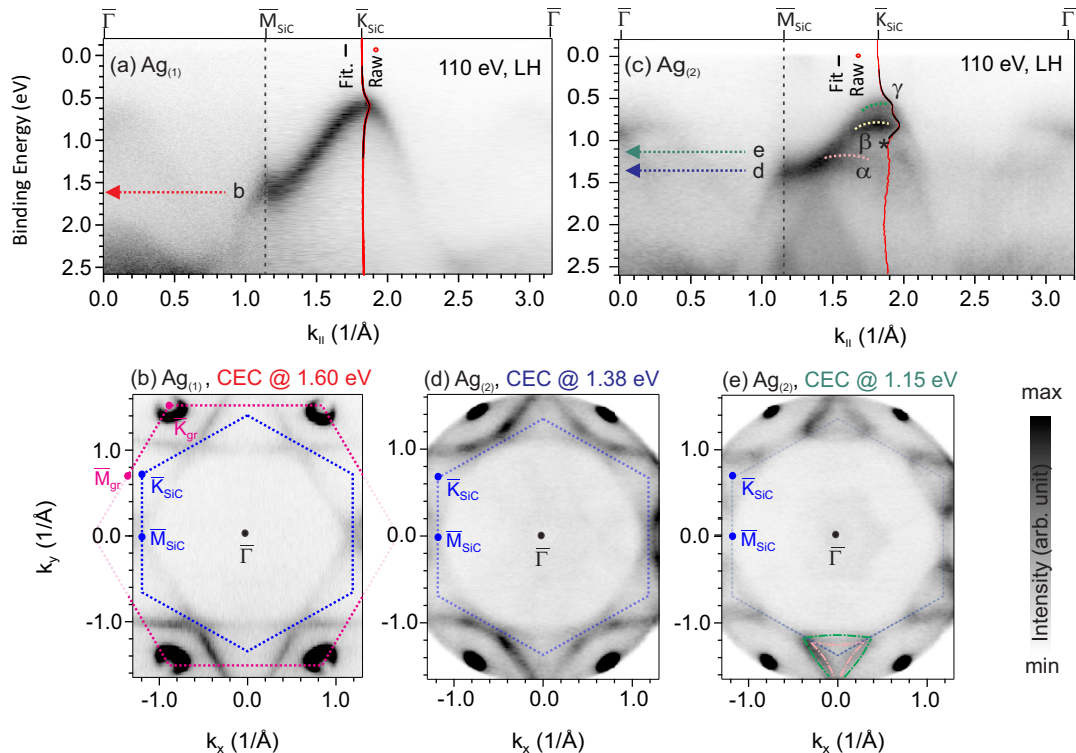


FIG. 2. E - k dispersions of (a) $\text{Ag}_{(1)}$ -QFMLG and (c) $\text{Ag}_{(2)}$ -QFMLG measured along the $\overline{\Gamma M_{\text{SiC}} \overline{K_{\text{SiC}}} \overline{\Gamma}}$ direction using 110 eV photons (with linear horizontal (LH) light, i.e., p-polarization). EDCs at $\overline{K_{\text{SiC}}}$ are overlaid in each panel (raw data: red points; Lorentzian fit: black line). The α , β , and γ band splitting, and the *-marked opening are discussed in the main text. (b) CEC of $\text{Ag}_{(1)}$ -QFMLG at a BE of 1.60 eV; the BZs of SiC (blue) and graphene (pink) are indicated. (d,e) CEC of $\text{Ag}_{(2)}$ -QFMLG at BEs of 1.38 eV and 1.15 eV, respectively; The CEC BEs are indicated in panels (a) and (c); two distinct $\text{Ag}_{(2)}$ pockets are highlighted in (e).

momentum. From this EDC fitting, the VBM is found at a BE of 0.57 ± 0.05 eV (associated with the γ branch), while the component with the highest spectral weight appears at 0.82 ± 0.05 eV (the β branch). Along $\overline{M_{\text{SiC}} \overline{K_{\text{SiC}}}}$ direction, the lowest-BE component is labeled as α . A gap-like suppression of spectral weight is observed between the β branch and the downward-dispersing branch along $\overline{K_{\text{SiC}}} \overline{\Gamma}$ at the position marked by ‘*’. A saddle-point feature is observed at the $\overline{M_{\text{SiC}}}$ point at a BE of approximately 1.40 eV. The CEC in Fig. 2(d) shows that, at the saddle point energy, the $\text{Ag}_{(2)}$ pockets exhibit a much weaker hexagonal warping as compared to $\text{Ag}_{(1)}$. A more detailed inspection also reveals two distinct Ag-derived pockets around $\overline{K_{\text{SiC}}}$ at a slightly higher BE, which are clearly resolved in the CEC at 1.15 eV BE in Fig. 2(e): the pocket outlined by the green dash-dotted line corresponds to the γ band, while the inner pocket marked in pink is associated with the α branch.

C. The periodicity in the k -space of $\text{Ag}_{(2)}$

Although the $\text{Ag}_{(2)}$ pockets are more circular overall, the momentum locations of the VBM and the saddle point remain the same as those of $\text{Ag}_{(1)}$. More importantly,

the periodicity in the k -space follows the BZ of the SiC, suggesting a (1×1) epitaxial relationship of $\text{Ag}_{(2)}$ with the SiC substrate. However, the structural model from Fig. 1(c) shows that the Ag unit cell in $\text{Ag}_{(2)}$ is 30° rotated with respect to the SiC unit cell, thus, the periodicity in the k -space is expected to follow the BZ indicated for the Ag (red) in Fig. 3(d). The apparent (1×1) -like symmetry in the ARPES data can be explained by the Ag-SiC interaction through inspecting the wavefunctions of the $\text{Ag}_{(2)}$ phase. For example, we can plot and compare the partial charge density at the VBM of the $\text{Ag}_{(1)}$ phase (Fig. 3(a-c)) and the $\text{Ag}_{(2)}$ phase (Fig. 3(e-g)). Although the wavefunction in $\text{Ag}_{(2)}$ has some charge density in the Ag layer, following the periodicity of the Ag lattice, the wavefunction is predominantly localized on the Si atoms, showing great similarity with that of the $\text{Ag}_{(1)}$ phase, therefore making the wavefunction more compatible with the SiC periodicity, meaning the VBM in $\text{Ag}_{(2)}$ should be better unfolded to the SiC primitive cell.

Computationally, to compare the calculated band structure of the $\text{Ag}_{(2)}$ phase (Fig. 3(e)) with the experimental ARPES data, the bands are first calculated in the BZ of the supercell (black in Fig. 3(d)), i.e., $(3\sqrt{3} \times 3\sqrt{3})$ -Ag on a (5×5) -SiC, and then unfolded to bands to a primitive cell [59]. Here, we have two options: the SiC primitive cell

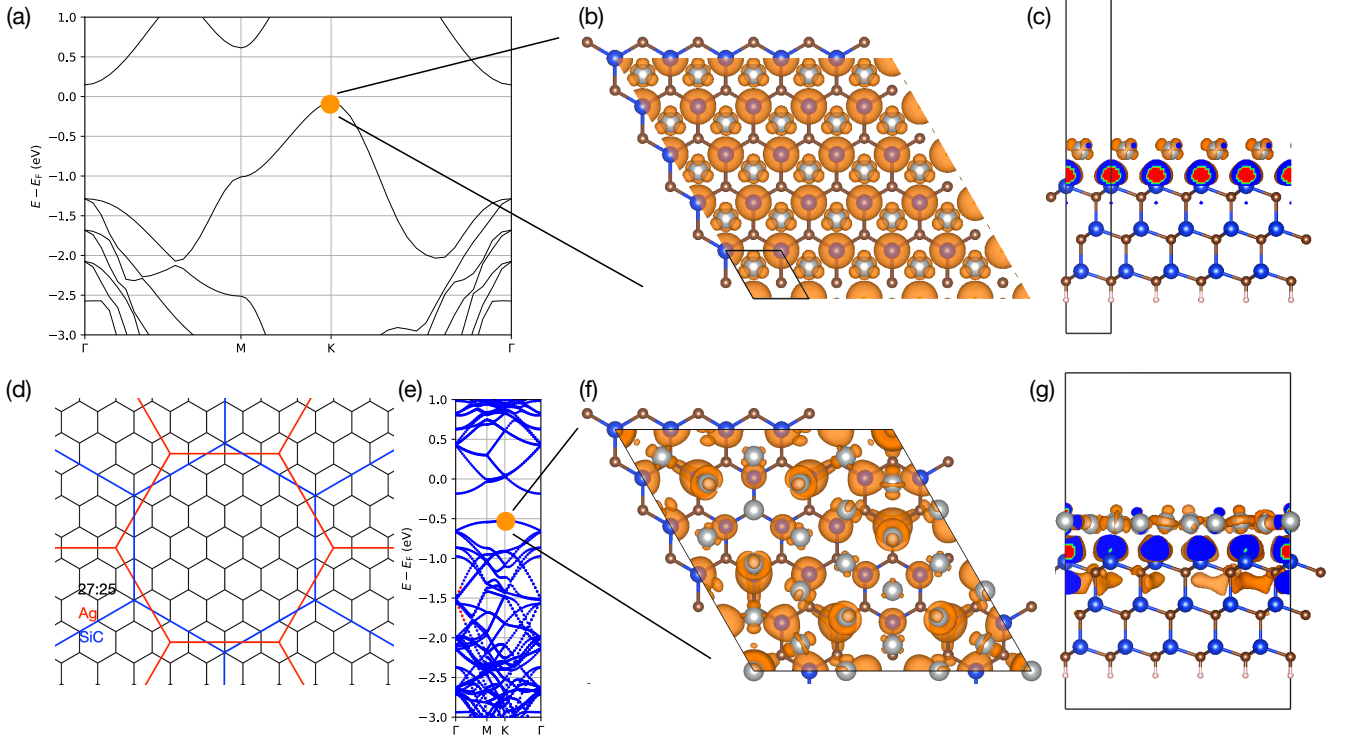


FIG. 3. (a) The band structure for the $\text{Ag}_{(1)}$ phase (with Ag atoms registered at the hollow site of the topmost SiC since it is the configuration with the lowest energy). (b) Top and (c) side view of the partial charge density of the state at the VBM (the orange dot) in (a). The orange color shows the shape of the isosurface while the red-to-blue color in the cross section shows the charge density distribution from high to low. (d) The Brillouin zones of the supercell for $\text{Ag}_{(2)}$ (black, marked as “27:25” for the Ag:SiC ratio), and the primitive Brillouin zones of the SiC (blue) and Ag (red) lattice. (e) The band structure for the supercell of the $\text{Ag}_{(2)}$ phase. The blue/red dots indicate that the corresponding state is more suitable to be unfolded to the SiC/Ag primitive cell, respectively, with a relatively smaller unfolding entropy as defined in Eq. (4). An example of a red dot would comparatively have more density in the Ag layer, and that part follows the periodicity of Ag (SI, section C, Fig. S3). (f) Top and (g) side view of the partial charge density of the state (color code as in panels (b,c)) at the VBM (the orange dot) in (e).

and the Ag primitive cell, and we need to decide which one is more suitable for the unfolding. For each electronic state $\mathbf{K}m$ in the supercell, the procedure of unfolding it to $\mathbf{k}_j m$ in the primitive cell (Eq. (14, 15) in Ref. [59]) is essentially to redistribute the spectral weight

$$1 = \sum_{\mathbf{G}} |C_{\mathbf{K}m}(\mathbf{G})|^2 \quad (1)$$

from the supercell first Brillouin zone (FBZ) to the primitive FBZ

$$P_{\mathbf{K}m}(\mathbf{k}_j = \mathbf{K} + \mathbf{G}_j) = \sum_{\mathbf{g}} |C_{\mathbf{K}m}(\mathbf{g} + \mathbf{G}_j)|^2 \quad (2)$$

$$\sum_j P_{\mathbf{K}m}(\mathbf{k}_j) = 1 \quad (3)$$

where m is the band index, C 's are Fourier coefficients, \mathbf{K} is a wavevector in the supercell FBZ, \mathbf{G} 's are reciprocal lattice vectors of the supercell, and their non-capital counterparts are for the primitive cell. For an ideal supercell created simply by multiplying a primitive cell, the unfolding of a non-degenerate state would yield a single

\mathbf{k}_j with $P_{\mathbf{K}m}(\mathbf{k}_j) = 1$. If we choose another primitive cell not compatible with the original one, we would have the spectral weight distributed over multiple \mathbf{k}_j 's, and the unfolding would be less meaningful. To quantify how well a state is compatible with a given primitive cell, we can define an unfolding entropy as

$$S_{\mathbf{K}m} = - \sum_j P_{\mathbf{K}m}(\mathbf{k}_j) \ln P_{\mathbf{K}m}(\mathbf{k}_j) \quad (4)$$

with a smaller value indicating a more meaningful unfolding, and the wavefunction more compatible with the chosen primitive cell, while a value of zero indicating a perfect unfolding. Applying this procedure to the $\text{Ag}_{(2)}$ supercell band structure (Fig. 3(e)), we find that most of the states near the VBM have a smaller unfolding entropy for the SiC primitive cell (blue dots) compared to the Ag primitive cell (red dots), indicating that for these states, they are more compatible with the periodicity of SiC, and the unfolding to the SiC primitive cell is more suitable for comparison with ARPES. The possible reason for this might be that the high energy dangling bonds of the topmost Si are more likely to capture most of the

bonding electrons when interacting with the 2D Ag. This could be seen that even at those red dots, we still have a significant contribution from the topmost Si (See SI, section C, Fig. S3).

D. Bands comparison between the theory and the experiment

We now turn to a detailed comparison between the experimental and theoretically calculated band dispersions of the $\text{Ag}_{(2)}$ phase in Fig. 4(a) (the corresponding analysis for $\text{Ag}_{(1)}$ is presented in SI, section D and Fig. S4). The calculated and unfolded bands are plotted along the $\overline{\Gamma\text{M}_{\text{SiC}}\text{K}_{\text{SiC}}\overline{\Gamma}}$ direction. Experimental data in the same direction was measured at 180 eV and shows essentially the same dispersion as the 110 eV data in Fig. 2(c) but has higher intensity. Overall, the DFT results reproduce the key experimental features with good agreement, including the dominant weakly dispersive (flat) β band and the downward-dispersing α branch in the vicinity of $\overline{\text{K}}_{\text{SiC}}$. We note that experimental intensities can vary depending on the momentum position of the measurement, e.g., first or repeated BZ (see SI, section E, Fig. S5). As mentioned in the Methods, we ignore the conduction bands and the position of the Fermi level in the calculated bands. By comparing with the unfolded DFT band structure (Fig. 4(a)), the “opening” (marked by ‘*’ in the figure) is not really the breaking of a single band, it is rather the intensity change of two bands in the supercell: Along the direction from $\overline{\text{K}}_{\text{SiC}}$ to $\overline{\Gamma}$, the β band loses intensity at the “opening”, while another band (downward branch) starts to show strong intensity there. This intensity suppression is a good example showing that the bands in ARPES are strongly influenced by the matrix element effects. In the calculation, the matrix element effect is partially captured by “absorbing the additional structure factor $\langle kn|Km\rangle$ ” between the supercell and primitive cell wavefunctions [70] through unfolding the supercell band structure properly to the SiC primitive cell. In Fig. 4(b), we compare the experimental CEC map at 1.35 eV BE with the CEC calculated from the unfolded $\text{Ag}_{(2)}$ DFT band structure at 0.05 eV below the saddle point at $\overline{\text{M}}_{\text{SiC}}$. The calculated contour reproduces the nearly circular $\text{Ag}_{(2)}$ pocket shape in good agreement with the experiment. To make the CEC better match the experimental data, the DFT CEC is broadened using a Lorentzian energy smearing of 0.1 eV and a Gaussian smearing of 0.06 \AA^{-1} along the momentum axes, followed by adjusting the intensity threshold. The calculated CEC with no smearing in the momentum plane and no intensity truncation is shown in Fig. S6 (d).

The uppermost γ branch at $\overline{\text{K}}_{\text{SiC}}$ and its continuation along $\overline{\text{K}}_{\text{SiC}}\overline{\Gamma}$ (better seen in Fig. 2(c)) are not captured by the $\text{Ag}_{(2)}$ -only calculation. Notably, these additional experimental features closely resemble the DFT band structure of the $\text{Ag}_{(1)}$ phase (see Fig. 4(c)). SI section G and Fig. S8 further analyzes the $\text{Ag}_{(1)}$ -like contribution observed in the experimental $\text{Ag}_{(2)}$ CEC. These obser-

vations suggest a residual mixture of the two phases in the sample, consistent with the phase coexistence inferred from the Ag $3d$ line-shape analysis in XPS. Nevertheless, the relative spectral weight of the Ag-derived states indicates that $\text{Ag}_{(2)}$ remains the predominant phase in the probed region.

E. Dirac cone dispersion of $\text{Ag}_{(1)}$ and $\text{Ag}_{(2)}$ -QFMLG

The denser lattice arrangement of the $\text{Ag}_{(2)}$ phase compared to $\text{Ag}_{(1)}$ not only produces a distinct electronic structure within the Ag monolayer itself, but is also expected to modify the electronic properties of the overlying graphene layer via proximity effects [71, 72]. To examine this, Fig. 5 compares the π -band dispersion of the QFMLG layer for samples intercalated in the $\text{Ag}_{(1)}$ and $\text{Ag}_{(2)}$ phases. Figures 5(a,b) show energy-momentum cuts through the graphene Dirac cone for $\text{Ag}_{(1)}$ -QFMLG and $\text{Ag}_{(2)}$ -QFMLG, respectively. The spectra were recorded at the graphene $\overline{\text{K}}_{\text{gr}}$ point along a momentum direction perpendicular to $\overline{\Gamma\text{K}}_{\text{gr}}$ using 40 eV photons. In both cases, the Dirac cone exhibits a characteristic renormalization near the Dirac point, manifested as an elongated crossing also known as a “diamond-like” dispersion [13]. This behavior is consistent with electron-plasmon coupling in graphene, which gives rise to plasmaron quasiparticles and produces two apparent branches: the “bare” Dirac dispersion (upper branch) and an interaction-renormalized (plasmaronic) dispersion with a Dirac-point shifted to lower BE [13, 73]. To extract the relevant energy scales, the dispersions of the upper π^* and lower π bands were fitted independently using momentum-distribution curves (MDCs); the resulting fits are shown by the red lines. Linear extrapolations of these fitted dispersions (white dashed lines) were then used to determine the Dirac-point energies associated with the bare Dirac cone, E_0 , and the plasmaronic branch, E_2 . For $\text{Ag}_{(1)}$ -QFMLG [Fig. 5(a)], the bare Dirac-point energy is $E_0 = 0.66 \pm 0.02$ eV below E_F , whereas for $\text{Ag}_{(2)}$ -QFMLG [Fig. 5(b)] it shifts to $E_0 = 0.77 \pm 0.02$ eV, indicating stronger n -type doping in the $\text{Ag}_{(2)}$ -intercalated sample.

A quantitative estimate of the carrier concentration was obtained from the Fermi surface contours shown in Fig. 5(c) ($\text{Ag}_{(1)}$ -QFMLG) and Fig. 5(d) ($\text{Ag}_{(2)}$ -QFMLG), which correspond to the π^* band pocket around $\overline{\text{K}}_{\text{gr}}$. Radial MDC fitting of the pocket was performed (red curve) to determine the enclosed area A . Using Luttinger’s theorem [74, 75], the electron density was evaluated from the Fermi surface area (for a spin- and valley-degenerate Dirac cone) as

$$n = \frac{g_s g_v A}{(2\pi)^2} = \frac{A}{\pi^2}, \quad (5)$$

where $g_s = 2$ and $g_v = 2$. This analysis yields $n \approx 3.38 \times 10^{13} \text{ cm}^{-2}$ for $\text{Ag}_{(1)}$ -QFMLG and $n \approx 5.92 \times 10^{13} \text{ cm}^{-2}$ for $\text{Ag}_{(2)}$ -QFMLG, confirming the higher electron doping

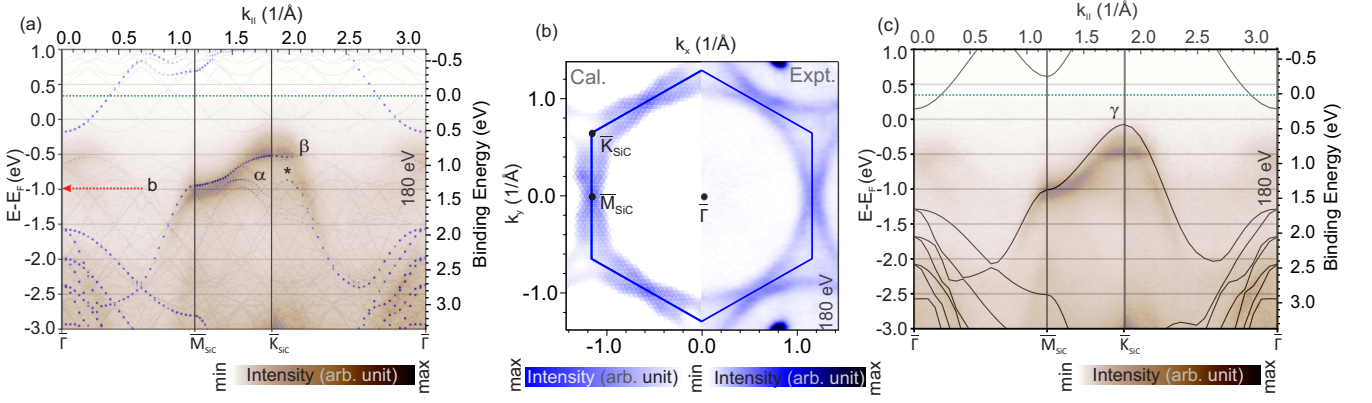


FIG. 4. Comparison of DFT and ARPES data. (a) DFT band structure of $\text{Ag}_{(2)}$ unfolded to SiC primitive cell (blue points) together with the corresponding folded supercell bands (transparent gray) along the $\overline{\Gamma M_{\text{SiC}} K_{\text{SiC}} \Gamma}$ direction; the ARPES spectrum measured at 180 eV is overlaid (in brown scale) for comparison. (b) Comparison of (left) the calculated CEC of the unfolded $\text{Ag}_{(2)}$ bands at 0.05 eV below the saddle point at $\overline{M}_{\text{SiC}}$ and (right) the experimental CEC at a BE of 1.35 eV. (c) DFT band structure of $\text{Ag}_{(1)}$ on SiC shown in the same format as in Fig. 3(a), stacked with the $\text{Ag}_{(2)}$ ARPES data along the $\overline{\Gamma M_{\text{SiC}} K_{\text{SiC}} \Gamma}$ direction; The experimental Fermi level is marked by the green dashed line in (a) and (c). The left and right y axes in (a) and (c) correspond to the calculated and experimental energy scales, respectively.

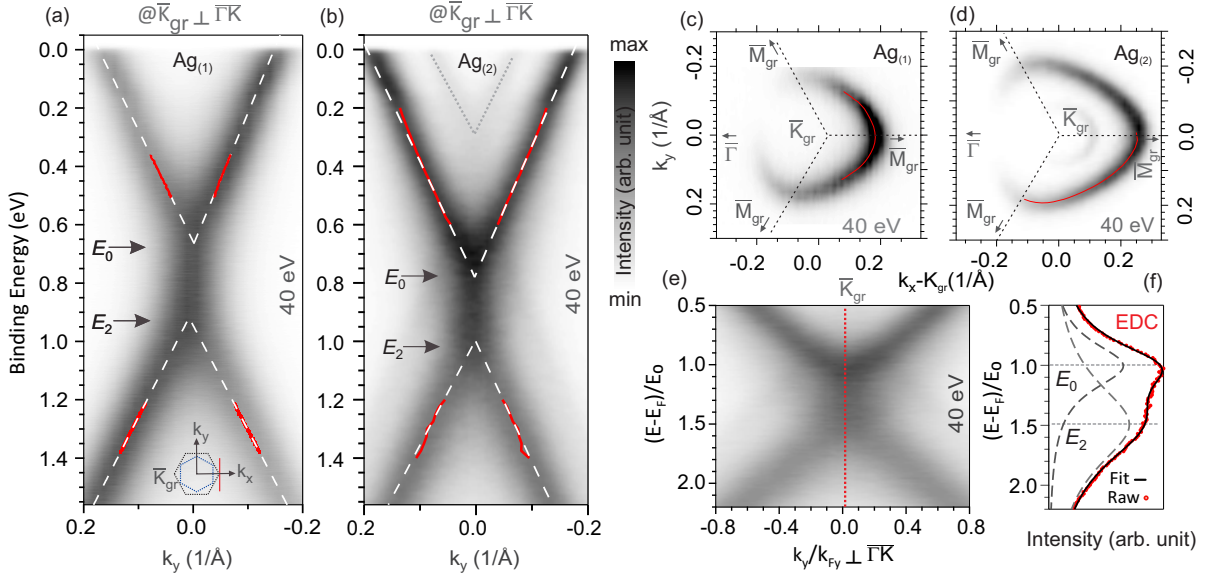


FIG. 5. (a) and (b) E - k cuts through the graphene Dirac cone at \overline{K}_{gr} for (a) $\text{Ag}_{(1)}$ -QFMLG and (b) $\text{Ag}_{(2)}$ -QFMLG, measured with photon energy 40 eV. MDC fits (red markers) and their linear extrapolations (white dashed lines) are used to determine the Dirac-points E_0 and E_2 . The measurement direction is indicated in the inset Brillouin zone map. (c) and (d) Fermi pockets associated with the Dirac cones of (c) $\text{Ag}_{(1)}$ -QFMLG and (d) $\text{Ag}_{(2)}$ -QFMLG; radial MDC fits are shown by the red curves. (e) Normalized (reduced-axis) representation of the $\text{Ag}_{(2)}$ -QFMLG Dirac-cone dispersion for analyzing the plasmaron-related “diamond” feature. (f) EDC (red dotted line) at \overline{K}_{gr} with Lorentzian fit (black line); the fitted components (gray dashed line) identify the bare and plasmaronic Dirac-points, E_0 and E_2 , respectively for $\text{Ag}_{(2)}$ -QFMLG.

in the $\text{Ag}_{(2)}$ -intercalated graphene. The enhanced n -type doping for $\text{Ag}_{(2)}$ -QFMLG is presumably caused by a more efficient charge transfer from the intercalated Ag layer to graphene. In particular, the reduced graphene- $\text{Ag}_{(2)}$ separation (as suggested by the XPS analysis and previously reported TEM results [35]) would strengthen the interfacial interaction and increase the net electron

transfer into the graphene π^* states, thereby shifting the Dirac point to higher BE. Note that the grey dashed cone in Fig. 5(b) and the extra faint inner pocket in Fig. 5(d) corresponds to monolayer graphene from the overgrown area of the sample.

We now analyze the pronounced elongation of the Dirac-point region in $\text{Ag}_{(2)}$ -QFMLG, which we attribute to the

intertwining of the plasmaronic Dirac cone (lower branch) with the bare Dirac cone (upper branch) of graphene. From the scaled energy separation between the Dirac points of the bare and plasmaronic bands, $\delta E = \left| \frac{E_2 - E_0}{E_0} \right|$, we determine the effective coupling constant, α_G of the graphene layer, following the one-particle Green's-function analysis within the G_0W -RPA framework [73]. In simple terms, a larger α_G corresponds to stronger electron-plasmon coupling in graphene. The normalized Dirac-cone dispersion of $\text{Ag}_{(2)}$ -QFMLG is shown in Fig. 5(e). The vertical axis is plotted as the scaled energy (δE) and the horizontal axis corresponds to the reduced Fermi momentum $k_y/k_{F,y}$. Here $k_{F,y}$ denotes the k_y value (at $k_x = K_{\text{gr}}$) where the π band crosses the Fermi level along the cut perpendicular to the $\overline{\Gamma K}_{\text{gr}}$ direction. For improved visibility of this crossing, Fig. 5(e) is shown over the 0.5–2.3 eV energy window. For the scaling we use the bare Dirac point energy $E_0 = 0.68 \pm 0.02$ eV obtained from an EDC analysis at \overline{K}_{gr} [Fig. 5(b) [76]], and $k_{F,y} = 0.18 \text{ \AA}^{-1}$. From the resulting plasmaron “diamond,” we extract $\delta E = 0.49 \pm 0.04$, which corresponds to an effective coupling constant of $\alpha_G \approx 0.5$ for $\text{Ag}_{(2)}$ -QFMLG. This value is larger than that obtained for $\text{Ag}_{(1)}$ -QFMLG [14], indicating stronger electron-plasmon coupling in the $\text{Ag}_{(2)}$ -intercalated system. Within this picture, the enhanced coupling is associated with a reduced dielectric screening provided by the $\text{Ag}_{(2)}/\text{SiC}$ environment. Using α_G , the effective dielectric constant of the $\text{Ag}_{(2)}/\text{SiC}$ medium can be estimated as $\epsilon_{\text{Ag}_{(2)}} \approx \frac{4.4}{\alpha_G} - 1$, which yields $\epsilon_{\text{Ag}_{(2)}} \approx 7.8$. This value is smaller than the corresponding estimate [77] for $\text{Ag}_{(1)}$ -QFMLG, $\epsilon_{\text{Ag}_{(1)}} \approx 10$, as shown in Ref.[14]. The reduced $\epsilon_{\text{Ag}_{(2)}}$ suggests weaker overall effective screening at the interface, which can be attributed to a more effective passivation of polarizable Si dangling-bond [13] states after $\text{Ag}_{(2)}$ intercalation on SiC compared to the $\text{Ag}_{(1)}/\text{SiC}$ interface.

F. Signature of band replicas in the $\text{Ag}_{(2)}$ intercalated QFMLG

The supercell periodicity in the $\text{Ag}_{(2)}$ -QFMLG, is also evident in replicated Dirac cone pockets, as shown in Fig. 6(a) by a wide-range Fermi surface map revealing such replicas surrounding the main graphene π^* pocket. This map is measured with 180 eV photon energy. The replica pockets are displaced relative to the main pocket along the graphene reciprocal-lattice directions by a small momentum separation, indicative of Umklapp scattering of the graphene π -bands by the superlattice reciprocal vector, \mathbf{G}_{sup} . To quantify the momentum separation, Fig. 6(b) shows a two-dimensional E - k cut extracted from Fig. 6(a) through \overline{K}_{gr} along a momentum direction perpendicular to $\overline{\Gamma K}_{\text{gr}}$. From the MDC in Fig. 6(c), obtained by integrating over the 0.85–0.95 eV BE window, we extract a supercell reciprocal-lattice vector magnitude of $|\mathbf{G}_{\text{sup}}| \approx 0.49 \text{ \AA}^{-1}$. This implies a real-space super-

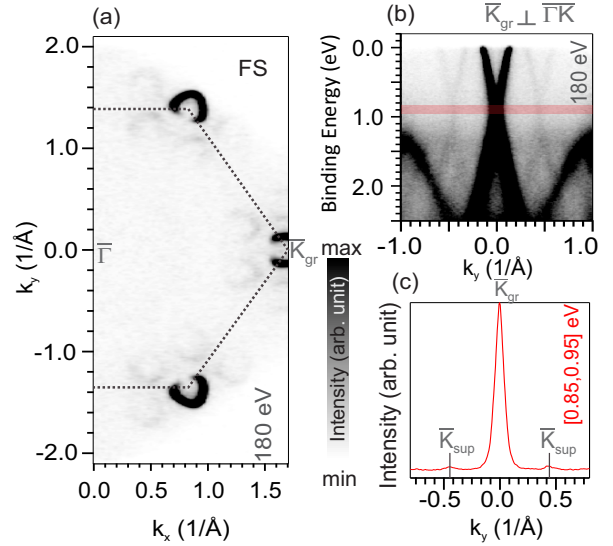


FIG. 6. (a) Fermi surface map of $\text{Ag}_{(2)}$ -QFMLG measured at 180 eV, highlighting replica pockets surrounding the main graphene Dirac-cone pocket. (b) E - k cut at \overline{K}_{gr} along a momentum direction perpendicular to $\overline{\Gamma K}_{\text{gr}}$, showing Dirac-cone replicas on both sides of the primary dispersion. (c) MDC integrated over the energy window indicated in (b), resolving the intense main peak of the Dirac cone at \overline{K}_{gr} and the replica features at $\overline{K}_{\text{sup}}$.

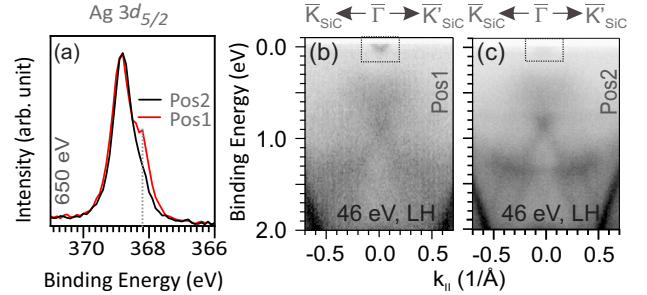


FIG. 7. (a) $\text{Ag } 3d_{5/2}$ XPS spectra of $\text{Ag}_{(2)}$ -QFMLG measured at 650 eV at two sample locations (Pos1 and Pos2). (b,c) ARPES spectra measured using 46 eV light (LH polarized) along the $\overline{K}_{\text{SiC}}\overline{\Gamma K}'_{\text{SiC}}$ direction at (b) Pos1 and (c) Pos2, highlighting the additional band crossing E_F at $\overline{\Gamma}$ in (b) that is absent in (c).

cell lattice constant of approximately six times that of graphene, consistent with the (6×6) coincidence supercell between $\text{Ag}_{(2)}$ and graphene inferred from the LEED data. Notably, no such replica pockets are observed for the $\text{Ag}_{(1)}$ -intercalated sample.

G. Spatial dependence of $\text{Ag}_{(2)}$

Finally, we address the origin of the lowest-BE shoulder observed in the $\text{Ag } 3d$ core-level spectrum of the $\text{Ag}_{(2)}$ -intercalated sample [Fig. 1(g-i)]. As argued above, this component likely originates from a distinct, spatially lo-

calized region within the intercalated Ag layer. To further test this interpretation, Fig. 7(a) compares the Ag $3d_{5/2}$ spectra measured at two different sample positions (Pos1 and Pos2) using the more surface-sensitive 450 eV excitation. A pronounced reduction of the shoulder intensity (BE position is marked by the dashed line) is observed when moving from Pos1 (the initial measurement position) to Pos2. We further compare ARPES spectra at the same positions using 46 eV photon energy, as shown in Fig. 7(b) and Fig. 7(c), respectively. At Pos1, an additional band crossing the E_F is clearly observed at the Γ point, whereas this feature is absent at Pos2. A closely related behavior has been reported for Au intercalation at the graphene/SiC interface, where intercalated monolayer Au yields a semiconducting dispersion, while intercalated bilayer Au produces an additional metallic band crossing E_F [23]. By analogy, we tentatively assign both the low-BE Ag $3d$ shoulder and the Γ -centered metallic band to regions containing a bilayer (or locally thicker) intercalated Ag phase. This assignment is also consistent with the magnitude of the core-level shift: the extra Ag $3d$ component is displaced by nearly ~ 1 eV to lower BE relative to the main Ag₍₂₎ $3d$ peak, comparable to the low-BE shift reported for Au. Note that in Fig. 7(b) and (c), the band near 1 eV BE at $\bar{\Gamma}$ corresponds to Ag replica bands, as discussed in detail in SI Section. F (Fig. S6 and S7). A question might arise whether such bilayer-like regions should also produce an observable change in the graphene doping level like Au-QFMLG. Here it is important to note that the spectral weight of the “bilayer” component is small: at Pos1 its intensity is below 15% of the total Ag₍₂₎ $3d$ intensity and appears confined to a highly localized region (of order $\sim 10 \mu\text{m}$) where both the strongest Γ -crossing band and the enhanced low-BE shoulder are detected. At other locations—representative of most of the sample—this fraction is even smaller, as indicated by Fig. 7(a) and Fig. 7(c). It is therefore likely that the majority of the ARPES data discussed above were acquired in regions where the bilayer contribution is negligible, consistent with the observation of a single Dirac cone characteristic of Ag₍₂₎-QFMLG with predominantly monolayer Ag intercalation. Enhancing and controlling the bilayer-like intercalated Ag contribution, and exploring the associated electronic properties, remains an open topic for future work.

IV. CONCLUSION

In summary, we show that changing the starting substrate from ZLG to Pb-QFMLG enables the formation of two distinct phases of intercalated 2D-Ag at the graphene/SiC interface under UHV conditions, and we provide a detailed structural and electronic property study of the second phase. LEED demonstrates that the Ag₍₂₎ layer is rotated by 30° with respect to the SiC substrate and forms supercells with both SiC ((5×5) periodicity) and graphene ((6×6) periodicity). Despite the rotated

Ag₍₂₎ lattice, high-resolution ARPES reveals a semiconducting Ag₍₂₎ band structure with the VBM at \bar{K}_{SiC} and a saddle point near \bar{M}_{SiC} , i.e., at momentum positions similar to those of the Ag₍₁₎ phase. The apparent similarity of the periodicity in the k -space between Ag₍₁₎ and Ag₍₂₎ is rationalized by DFT: By defining the unfolding entropy, we find that, in a quantified way, for Ag₍₂₎, the SiC unit cell, instead of the Ag unit cell, is more suitable for most of the electronic states near VBM to be unfolded to. This means that those electronic states have a major part with the periodicity compatible to the SiC substrate, therefore making the unfolded bands have the Ag₍₁₎ (or SiC) periodicity in the k -space. The calculated band structure based on the Ag₍₂₎ structural model is in good agreement with the experimentally observed dispersion. Importantly, we also find that these two Ag phases tune the electronic properties of the overlying graphene layer differently. Ag₍₂₎ produces stronger n -type doping in QFMLG and enhances the plasmaron-related renormalization of the Dirac point, reflected in an increase of the effective coupling constant from $\alpha_G \approx 0.4$ (Ag₍₁₎) to $\alpha_G \approx 0.5$ (Ag₍₂₎), consistent with a smaller effective dielectric constant of the Ag₍₂₎/SiC layers. In addition, ARPES resolves (6×6) Dirac-cone replica pockets for Ag₍₂₎-QFMLG, providing a more precise quantitative confirmation of the graphene/Ag₍₂₎ supercell inferred from LEED.

More broadly, our results demonstrate that modifying the defect density of the initial substrate can stabilize different intercalated phases under UHV conditions. This provides a practical pathway to access and compare multiple 2D phases for other intercalants as well. Since the graphene doping level and many-body renormalizations depend strongly on the specific intercalated phase, controlling the phase of the confined layer is not only essential for fundamental studies but also critical for applications that rely on reproducible electronic tuning.

V. ACKNOWLEDGEMENTS

S.D. K.K. and U.St. acknowledge support from the Deutsche Forschungsgemeinschaft (DFG, German Research Foundation) within Research Unit FOR5242 (Project Sta315/13-1 and Ku4228/1-1). B.Z. and V.H.C. thank the support from Two-Dimensional Crystal Consortium-Materials Innovation Platform (2DCC-MIP) under NSF cooperative agreement no. DMR-2039351. A.J. and J.A.R. acknowledge the support from National Science Foundation (NSF) award no. DMR-2011839, through the Penn State MRSEC—Center for Nanoscale Science. We acknowledge MAX IV Laboratory for beamtime at the BLOCH beamline under Proposal No. 20241262, and Helmholtz-Zentrum Berlin for beamtime at the UE112-PGM-2a-1² beamline under Proposal No. Photons-231-12042. We thank Dr. Nisha Ranjan and Ms. Vibha Reddy (MPI-FKF), Dr. Jacek Osiecki (BLOCH beamline), Dr. Andrei Varykhalov (UE112-PGM-2a-1² beamline),

and the beamline staff at BLOCH and UE112-PGM-2a-1² for their assistance during the beamtimes. We also thank Ms. Bharti Matta (MPI-FKF) for helpful discussions related to the experimental data analysis. A.J. and J.A.R. would like to acknowledge Li-Syuan Lu, Chengye Dong and Shengxi Huang for fruitful discussions during

the experimental design. Research conducted at MAX IV, a Swedish national user facility, is supported by the Swedish Research council under contract 2018-07152, the Swedish Governmental Agency for Innovation Systems under contract 2018-04969, and Formas under contract 2019-02496.

-
- [1] K. S. Novoselov, A. K. Geim, S. V. Morozov, D. Jiang, Y. Zhang, S. V. Dubonos, I. V. Grigorieva, and A. A. Firsov, *Science* **306**, 666 (2004).
- [2] A. K. Geim and K. S. Novoselov, *Nat. Mater.* **6**, 183 (2007).
- [3] Y.-W. Son, M. L. Cohen, and S. G. Louie, *Phys. Rev. Lett.* **97**, 216803 (2006).
- [4] G. R. Bhimanapati, Z. Lin, V. Meunier, Y. Jung, J. Cha, S. Das, D. Xiao, Y. Son, M. S. Strano, V. R. Cooper, L. Liang, S. G. Louie, E. Ringe, W. Zhou, S. S. Kim, R. R. Naik, B. G. Sumpter, H. Terrones, F. Xia, Y. Wang, J. Zhu, D. Akinwande, N. Alem, J. A. Schuller, R. E. Schaak, M. Terrones, and J. A. Robinson, *ACS Nano* **9**, 11509 (2015).
- [5] Z. Lin, A. McCreary, N. Briggs, S. Subramanian, K. Zhang, Y. Sun, X. Li, N. J. Borys, H. Yuan, S. K. Fullerton-Shirey, A. Chernikov, H. Zhao, S. McDonnell, A. M. Lindenberg, K. Xiao, B. J. LeRoy, M. Drndić, J. C. M. Hwang, J. Park, M. Chhowalla, R. E. Schaak, A. Javey, M. C. Hersam, J. Robinson, and M. Terrones, *2D Mater.* **3**, 042001 (2016).
- [6] D. Bera, L. Qian, T. Tseng, and P. H. Holloway, *Materials (Basel)* **3**, 2260 (2010).
- [7] X. Huang, C. Liu, and P. Zhou, *npj 2D Mater. Appl.* **6**, 51 (2022).
- [8] K. S. Novoselov, A. K. Geim, S. V. Morozov, D. Jiang, M. I. Katsnelson, I. V. Grigorieva, S. V. Dubonos, and A. A. Firsov, *Proc. Natl. Acad. Sci.* **102**, 10451 (2005).
- [9] H. Karakachian, T. T. N. Nguyen, J. Aprozanz, A. A. Zakharov, R. Yakimova, P. Rosenzweig, C. M. Polley, T. Balasubramanian, C. Tegenkamp, S. R. Power, and U. Starke, *Nat. Commun.* **11**, 6380 (2020).
- [10] E. Parzinger, E. Mitterreiter, M. Stelzer, F. Kreupl, J. W. Ager, A. W. Holleitner, and U. Wurstbauer, *Appl. Mater. Today* **8**, 132 (2017).
- [11] C. Lee, X. Wei, J. W. Kysar, and J. Hone, *Science* **321**, 385 (2008).
- [12] K. F. Mak, C. Lee, J. Hone, J. Shan, and T. F. Heinz, *Phys. Rev. Lett.* **105**, 136805 (2010).
- [13] A. Bostwick, F. Speck, T. Seyller, K. Horn, and E. Rotenberg, *Science* **328**, 999 (2010).
- [14] P. Rosenzweig, H. Karakachian, D. Marchenko, and U. Starke, *Phys. Rev. B* **105**, 235428 (2022).
- [15] S. Link, S. Forti, A. Stöhr, K. Küster, M. Rösner, D. Hirschmeier, C. Chen, J. Avila, M. C. Asensio, A. A. Zakharov, T. O. Wehling, A. I. Lichtenstein, M. I. Katsnelson, and U. Starke, *Phys. Rev. B* **100**, 121407 (2019).
- [16] S. A. Herrera, G. Parra-Martínez, P. Rosenzweig, B. Matta, C. M. Polley, K. Küster, U. Starke, F. Guinea, J. Á. Silva-Guillén, G. G. Naumis, and P. A. Pantaleón, *ACS Nano* **18**, 34842 (2024).
- [17] Q. Zhong, J. Zhang, P. Cheng, B. Feng, W. Li, S. Sheng, H. Li, S. Meng, L. Chen, and K. Wu, *J. Phys.: Condens. Matter* **29**, 095002 (2017).
- [18] K. Romanyuk, J. Brona, and B. Voigtländer, *Phys. Rev. Lett.* **103**, 096101 (2009).
- [19] M. Körner, F. Loske, M. Einax, A. Kühnle, M. Reichling, and P. Maass, *Phys. Rev. Lett.* **107**, 016101 (2011).
- [20] T. Aizawa, S. Suehara, and S. Otani, *J. Phys. Chem. C* **118**, 23049 (2014).
- [21] C. Riedl, C. Coletti, T. Iwasaki, A. A. Zakharov, and U. Starke, *Phys. Rev. Lett.* **103**, 246804 (2009).
- [22] K. V. Emtsev, A. A. Zakharov, C. Coletti, S. Forti, and U. Starke, *Phys. Rev. B* **84**, 125423 (2011).
- [23] S. Forti, S. Link, A. Stöhr, Y. Niu, A. A. Zakharov, C. Coletti, and U. Starke, *Nat. Commun.* **11**, 2236 (2020).
- [24] P. Rosenzweig and U. Starke, *Phys. Rev. B* **101**, 201407 (2020).
- [25] B. Matta, P. Rosenzweig, O. Bolkenbaas, K. Küster, and U. Starke, *Phys. Rev. Res.* **4**, 023250 (2022).
- [26] Z. Y. Al Balushi, K. Wang, R. K. Ghosh, R. A. Vilá, S. M. Eichfeld, J. D. Caldwell, X. Qin, Y.-C. Lin, P. A. DeSario, G. Stone, S. Subramanian, D. F. Paul, R. M. Wallace, S. Datta, J. Redwing, and J. A. Robinson, *Nat. Mater.* **15**, 1166 (2016).
- [27] H. El-Sherif, N. Briggs, B. Bersch, M. Pan, M. Hamidinejad, S. Rajabpour, T. Filleter, K. W. Kim, J. Robinson, and N. D. Bassim, *ACS Appl. Mater. Interfaces* **13**, 55428 (2021).
- [28] A. Vera, B. Zheng, W. Yanez, K. Yang, S. Y. Kim, X. Wang, J. C. Kotsakidis, H. El-Sherif, G. Krishnan, R. J. Koch, T. A. Bowen, C. Dong, Y. Wang, M. Wetherington, E. Rotenberg, N. Bassim, A. L. Friedman, R. M. Wallace, C. Liu, N. Samarth, V. H. Crespi, and J. A. Robinson, *ACS Nano* **18**, 21985 (2024).
- [29] S. Wundrack, M. Bothe, M. Jaime, K. Küster, M. Gruschwitz, Y. Yin, Z. Mamiyev, P. Schädlich, B. Matta, S. Datta, M. Eckert, C. Tegenkamp, U. Starke, R. Stosch, H. W. Schumacher, T. Seyller, K. Pierz, T. Tschirner, and A. Bakin, *Adv. Mater.* **38**, e11992 (2026).
- [30] L.-S. Lu, A. Vera, F. Turker, K. M. Ananthanarayanan, C. Dong, M. Wetherington, and J. A. Robinson, *J. Vac. Sci. Technol. A* **44**, 030802 (2026).
- [31] E. Pompei, K. Skibińska, G. Senesi, Y. Vlamidis, A. Rossi, S. Forti, C. Coletti, F. Beltram, S. Rubini, L. Sorba, S. Heun, and S. Veronesi, *Small* **21**, e05640 (2025).
- [32] N. Briggs, B. Bersch, Y. Wang, J. Jiang, R. J. Koch, N. Nayir, K. Wang, M. Kolmer, W. Ko, A. De La Fuente Duran, S. Subramanian, C. Dong, J. Shallenberger, M. Fu, Q. Zou, Y.-W. Chuang, Z. Gai, A.-P. Li, A. Bostwick, C. Jozwiak, C.-Z. Chang, E. Rotenberg, J. Zhu, A. C. T. van Duin, V. Crespi, and J. A. Robinson, *Nat. Mater.* **19**, 637 (2020).
- [33] M. T. Wetherington, F. Turker, T. Bowen, A. Vera, S. Rajabpour, N. Briggs, S. Subramanian, A. Maloney, and J. A. Robinson, *2D Mater.* **8**, 041003 (2021).

- [34] K. Zhang, R. A. Maniyara, Y. Wang, A. Jain, M. T. Wetherington, T. T. Mai, C. Dong, T. Bowen, K. Wang, S. V. Rotkin, A. R. H. Walker, V. H. Crespi, J. Robinson, and S. Huang, *Sci. Adv.* **11**, eadw1800 (2025).
- [35] A. Jain, B. Zheng, S. Datta, K. Ulman, J. Henz, M. W.-J. Liu, V. D. Pham, W. He, C. Dong, L.-S. Lu, A. Vera, N. Sawtarie, W. Aufer, K. Wang, B. Hengstebeck, Z. W. Henshaw, S. Mathela, M. T. Wetherington, W. H. Blades, K. Knappenberger, U. Wurstbauer, S. Y. Quek, U. Starke, S. Huang, V. H. Crespi, and J. A. Robinson, *arXiv* (2025), [arXiv:2511.07151](https://arxiv.org/abs/2511.07151) [cond-mat.mtrl-sci].
- [36] M. W.-J. Liu, K. A. Ulman, B. Zheng, A. Jain, D. J. Heintzelman, K. Wang, W. He, C. Dong, L.-S. Lu, V. H. Crespi, S. Y. Quek, J. A. Robinson, and K. L. J. Knappenberger, *Nano Letters* **25**, 17145 (2025).
- [37] C. Dong, L.-S. Lu, Y.-C. Lin, and J. A. Robinson, *ACS Nanoscience Au* **4**, 115 (2024).
- [38] V. Ramachandran, M. F. Brady, A. R. Smith, R. M. Feenstra, and D. W. Greve, *J. Electron. Mater.* **27**, 308 (1998).
- [39] S. Soubatch, S. E. Sadow, S. P. Rao, W. Lee, M. Konuma, and U. Starke, *Mater. Sci. Forum* **483**, 761 (2005).
- [40] K. V. Emtsev, A. Bostwick, K. Horn, J. Jobst, G. L. Kellogg, L. Ley, J. L. McChesney, T. Ohta, S. A. Reshanov, J. Röhrli, E. Rotenberg, A. K. Schmid, D. Waldmann, H. B. Weber, and T. Seyller, *Nat. Mater.* **8**, 203 (2009).
- [41] C. Riedl, C. Coletti, and U. Starke, *J. Phys. D: Appl. Phys.* **43**, 374009 (2010).
- [42] S. Forti and U. Starke, *J. Phys. D: Appl. Phys.* **47**, 094013 (2014).
- [43] K. V. Emtsev, F. Speck, T. Seyller, L. Ley, and J. D. Riley, *Phys. Rev. B* **77**, 155303 (2008).
- [44] Y. Liu, X. Liu, C.-Z. Wang, Y. Han, J. W. Evans, A. Li-Rosales, M. C. Tringides, and P. A. Thiel, *J. Phys. Chem. C* **125**, 6954 (2021).
- [45] B. Matta, P. Rosenzweig, K. Küster, C. Polley, and U. Starke, *Phys. Rev. B* **111**, 155435 (2025).
- [46] S. Fiori, Y. Murata, S. Veronesi, A. Rossi, C. Coletti, and S. Heun, *Phys. Rev. B* **96**, 125429 (2017).
- [47] P. Schädlich, C. Ghosal, M. Stettner, B. Matta, S. Wolff, F. Schölzel, P. Richter, M. Hutter, A. Haags, S. Wenzel, Z. Mamiyev, J. Koch, S. Soubatch, P. Rosenzweig, C. Polley, F. S. Tautz, C. Kumpf, K. Küster, U. Starke, T. Seyller, F. C. Bocquet, and C. Tegenkamp, *Adv. Mater. Interfaces* **10**, 2300471 (2023).
- [48] S. Chen, P. A. Thiel, E. Conrad, and M. C. Tringides, *Phys. Rev. Mater.* **4**, 124005 (2020).
- [49] C. M. Polley, M. Leandersson, J. Adell, J. Osiecki, D. Carbone, K. Ali, H. Fedderwitz, and T. Balasubramanian, *Synchrotron Radiat. News* **37**, 18 (2024).
- [50] A. Varykhalov, *J. Large-Scale Res. Facil.* **4**, A99 (2018).
- [51] G. Kresse and J. Furthmüller, *Comput. Mater. Sci.* **6**, 15 (1996).
- [52] G. Kresse and J. Furthmüller, *Phys. Rev. B* **54**, 11169 (1996).
- [53] G. Kresse and J. Hafner, *Phys. Rev. B* **47**, 558 (1993).
- [54] G. Kresse and D. Joubert, *Phys. Rev. B* **59**, 1758 (1999).
- [55] P. E. Blöchl, *Phys. Rev. B* **50**, 17953 (1994).
- [56] J. P. Perdew, K. Burke, and M. Ernzerhof, *Phys. Rev. Lett.* **77**, 3865 (1996).
- [57] S. Grimme, J. Antony, S. Ehrlich, and H. Krieg, *J. Chem. Phys.* **132**, 154104 (2010).
- [58] S. Grimme, S. Ehrlich, and L. Goerigk, *J. Comput. Chem.* **32**, 1456 (2011).
- [59] V. Popescu and A. Zunger, *Phys. Rev. B* **85**, 085201 (2012).
- [60] Q. Zheng, *VaspBandUnfolding* (2026).
- [61] J. P. Perdew, *Int. J. Quantum Chem.* **28**, 497 (1985).
- [62] M. P. Seah and W. A. Dench, *Surf. Interface Anal.* **1**, 2 (1979).
- [63] U. Starke and C. Riedl, *J. Phys.: Condens. Matter* **21**, 134016 (2009).
- [64] V. D. Pham, B. Zheng, A. Jain, C. Dong, L.-S. Lu, Z. W. Henshaw, W. H. Blades, J. A. Robinson, V. H. Crespi, A. Trampert, and R. Engel-Herbert, *Phys. Rev. Mater.* **10**, 034003 (2026).
- [65] J. A. Bearden and A. F. Burr, *Rev. Mod. Phys.* **39**, 125 (1967).
- [66] J. Yu, S. Ye, X. Xv, L. Pan, P. Lin, H. Liao, and D. Wang, *Nanomaterials* **12**, 3215 (2022).
- [67] J. J. Yeh and I. Lindau, *At. Data Nucl. Data Tables* **32**, 1 (1985).
- [68] J. J. Olivero and R. L. Longbothum, *J. Quant. Spectrosc. Radiat. Transfer* **17**, 233 (1977).
- [69] W. Lee, Y. Wang, W. Qin, H. Kim, M. Liu, T. N. Nunley, B. Fang, R. Maniyara, C. Dong, J. A. Robinson, V. H. Crespi, X. Li, A. H. MacDonald, and C.-K. Shih, *Nano Letters* **22**, 7841 (2022).
- [70] W. Ku, T. Berlijn, and C.-C. Lee, *Phys. Rev. Lett.* **104**, 216401 (2010).
- [71] P. Rosenzweig, H. Karakachian, D. Marchenko, K. Küster, and U. Starke, *Phys. Rev. Lett.* **125**, 176403 (2020).
- [72] B. Matta, P. Rosenzweig, C. Polley, U. Starke, and K. Küster, *Nanoscale* **17**, 19317 (2025).
- [73] A. L. Walter, A. Bostwick, K.-J. Jeon, F. Speck, M. Ostler, T. Seyller, L. Moreschini, Y. J. Chang, M. Polini, R. Asgari, A. H. MacDonald, K. Horn, and E. Rotenberg, *Phys. Rev. B* **84**, 085410 (2011).
- [74] J. M. Luttinger and J. C. Ward, *Phys. Rev.* **118**, 1417 (1960).
- [75] J. M. Luttinger, *Phys. Rev.* **119**, 1153 (1960).
- [76] We note a small difference in the extracted bare Dirac point energy depending on the analysis method: linear extrapolation of the MDC-derived dispersion yields $E_0 = 0.77$ eV, whereas the EDC analysis gives $E_0 = 0.68$ eV. For the determination width of the diamond, we follow the standard procedure and normalize using the E_0 value obtained from the EDC analysis. The discrepancy between the two estimates is likely related to the strong plasmaron-induced renormalization in the immediate vicinity of the Dirac point, which can shift the apparent crossing in linear extrapolations. A similar offset of E_0 values is also observed for the $\text{Ag}_{(1)}$ -intercalated sample. (.)
- [77] For $\text{Ag}_{(1)}$ -QFMLG, the Dirac points extracted from our MDC-based linear extrapolation, E_0 and E_2 , are consistent with the values reported in Ref. [14]. However, due to experimental constraints in the present measurements, the Dirac cone features are broader, which reduces the precision of the normalized plasmaron-diamond analysis and the resulting plasmaron width. Since E_0 and E_2 agree with Ref. [14], we assume the corresponding plasmaron width to be unchanged and therefore adopt the same effective coupling constant α_G and dielectric constant $\epsilon_{\text{Ag}(1)}$ as reported there. (.)